#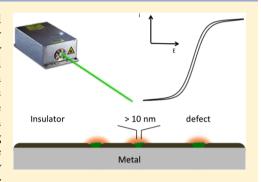 Observation of Nanometer-Sized Electro-Active Defects in Insulating Layers by Fluorescence Microscopy and Electrochemistry

Christophe Renault,[†,‡] Kyle Marchuk,[†,‡] Hyun S. Ahn,[‡] Eric J. Titus,[‡] Jiyeon Kim,[‡] Katherine A. Willets,*[,‡,§] and Allen J. Bard*[,‡]

[‡]Center for Electrochemistry, Department of Chemistry, The University of Texas at Austin, Austin, Texas 78712, United States

S *Supporting Information*

ABSTRACT: We report a method to study electro-active defects in passivated electrodes. This method couples fluorescence microscopy and electrochemistry to localize and size electro-active defects. The method was validated by comparison with a scanning probe technique, scanning electrochemical microscopy. We used our method for studying electro-active defects in thin TiO_2 layers electrodeposited on 25 μm diameter Pt ultramicroelectrodes (UMEs). The permeability of the TiO_2 layer was estimated by measuring the oxidation of ferrocenemethanol at the UME. Blocking of current ranging from 91.4 to 99.8% was achieved. Electro-active defects with an average radius ranging between 9 and 90 nm were observed in these TiO_2 blocking layers. The distribution of electro-active defects over the TiO_2 layer is highly inhomogeneous and the number of electro-active defect increases for lower degree of current blocking. The interest of the proposed technique is the possibility to quickly (less than 15 min) image samples as large as several hundreds of μm^2 while being able to detect electro-active defects of only a few tens of nm in radius.

W̲e report a method to study electro-active defects in passivated electrodes. This method couples fluorescence microscopy and electrochemistry to localize and size electro-active defects. Interestingly, the proposed technique has the potential to quickly image sample sizes of hundreds of μm^2 while detecting electro-active defects of only a few tens of nm in diameter.

Conducting surfaces partially or completely insulated by thin dielectric layers are important because they are employed in multiple key applications such as electronic components,[1−5] photocatalytic devices,[6−10] and biological sensors[11,12] and are also widely used to prevent the corrosion of metals.[13,14] For the aforementioned applications, the quality of the layer and, more particularly, the presence of electro-active defects is critical. These electro-active defects can be pinholes as well as conducting impurities in the insulating layer. Electrochemistry is a particularly well-suited analytical tool for the study of electro-active defects since electro-active surfaces as small as a few nanometers in diameter can generate measurable currents (pA). For example, Satpati et al. used cyclic voltammetry and chronoamperometry to demonstrate the presence of electro-active defects smaller than a micron in a several nanometer thick layer of TiO_2 deposited by atomic layer deposition on indium tin oxide.[15] To obtain information on the location and size of individual electro-active defects, scanning probe techniques can be used. The scanning vibrating electrode technique,[16] scanning Kelvin probe microscopy,[17] and localized electrochemical impedance spectroscopy[18] have been largely used for studying micron-sized electro-active defects occurring during corrosion of metals. Higher spatial resolution was

achieved with conducting atomic force microscopy (c-AFM) and electro-active defects of only few nanometers in 100 nm thick films of AlO_x could be imaged.[19] C-AFM can also be performed in solution. For example, c-AFM was employed to image in generation-collection mode an array of 1 μm diameter electrodes with a resolution of 50 nm.[20] Scanning tunneling microscopy has been used by Sun et al. to image electro-active defects of 2 to 5 nm in diameter in alkylthiol self-assembled monolayers.[21] Such high resolution was enabled by under-potential deposition of copper in the electro-active defects. Scanning electrochemical microscopy (SECM) along with ultramicroelectrodes (UMEs) has also been largely used to image the electro-activity of surfaces.[22−24] White and co-workers used SECM to study corrosion in thin native oxide films of TiO_2,[25] Ta_2O_5[26] and Al_2O_3.[27] Electro-active defects of a few μm were imaged in a 2−3 nm thick Al_2O_3 insulating layer.[28]

While scanning probe techniques can reveal spatial information compared to regular electrochemistry, they have some inherent limitations. To achieve higher imaging resolution, smaller tip sizes must be used, which decreases the area imaged or increases the time required to map a certain area. This can lead to imaging times of hours to investigate even modest samples sizes (~100 μm^2). In addition, high-resolution probes tend to be very delicate and are prone to dulling in the case of AFM and breaking in the case of SECM. For example,

to achieve nm scale resolution in SECM, nm -sized probes need to be brought within tens of nanometers of the surface before imaging. This approach can easily result in a broken tip if alignment is even slightly off or there is any drift in the sample. Moreover, the roughness of the sample has to be relatively low to limit the risk of crashing probes with the sample.

To overcome these limitations while maintaining nanoscale spatial resolution, we demonstrate a far-field optical imaging technique to rapidly image submicron size electro-active defects over large areas. This technique uses wide-field fluorescence microscopy in combination with traditional electrochemistry. First, a redox-active fluorescent dye is reduced at the site of electro-active defects on a passivated electrode surface. Upon reduction the dye becomes fluorescent and insoluble, depositing fluorescent islands that identify the locations of the electro-active defects. Fluorescence microscopy is then used to provide a rapid estimation of the number and position of electro-active defects. Utilizing a complementary character-ization of the sample by cyclic voltammetry allows for an average size estimate of the electro-active defects. This complementary technique can spatially resolve defects that are much smaller than the diffraction limit of light on samples hundreds of microns in area. The imaging is simple, fast and can be performed on rough surfaces without sacrificing spatial resolution. This spectroelectrochemical technique offers a simple alternative to time intensive complex techniques such as c-AFM and SECM.

■ EXPERIMENTAL SECTION

Chemicals and Materials. 5-Cyano-2,3-di(p-tolyl) tetra-zolium chloride (CTC, ≥85%), 1,1′-ferrocenedimethanol (FcDM, 97%), 1-ferrocenemethanol (FcMeOH, 98%), and titanium(III) chloride (12% in HCl) were purchased from Sigma-Aldrich (St Louis, MO). Potassium nitrate, potassium phosphate, sulfuric acid (95−98%w/w), hydrogen peroxide (30%), hydrochloric acid (12.5 N), sodium bicarbonate, and 5 min epoxy were purchased from Fisher (Waltham, MA). All solutions were prepared with DI water (18 MΩ·cm) from a Milli-Q water system from Millipore (Billerica, MA). Diamond paper (0.1 μm) grit was purchased from Allied High Tech Product Inc. (Rancho Dominguez, CA). The Au (10 μm diameter, annealed) and Pt (25 μm diameter, annealed) wires were purchased from Alfa Aeser, and the capillaries (borosilicate, ID = 0.5 mm OD = 1.5 mm) were purchased from Sutter Instrument (Novato, CA). The silver epoxy (H2OE Epo-tek) was purchased from Ted Pella, Inc. (Redding, CA). The UMEs were fabricated by heat-sealing a metal wire (Au or Pt) in a glass capillary. The electric connection between the metal wire and the lead of the potentiostat was established with a 0.25 mm diameter wire and silver epoxy. A regular epoxy was used to firmly maintain the wire in the capillary.

Electrochemical Measurements. Cyclic voltammetry of CTC was performed using a CH760E potentiostat from CH Instruments (Austin, TX), a 1 mm diameter Pt working electrode, a Pt wire counter electrode, and a Ag/AgCl KCl 1 M reference electrode. The working electrode was polished with 1 μm and 0.05 μm alumina and then sonicated in water and ethanol prior to the experiment. The SECM experiments were carried out with a CH920C system from CH Instruments. Briefly, a 10 μm diameter Au UME with a RG (radius of electrode, metal and glass sheath, divided by radius of the metal wire) of 2−3 was used to image the surface of the 25 μm diameter Pt UME. The redox probe was FcDM at ≈5 mM in an

aqueous solution containing 0.1 M of KNO_3 as supporting electrolyte. The tip was approached at 0.2 μm/s and stopped a few μm from the surface of the substrate. The tip−substrate distance was measured in negative feedback mode on the insulating glass sheath. In addition to the imaging of the Pt electrode, an image of the glass sheath was taken to identify the angular position of the electrode and compare with fluorescence micrographs. Stepper motors were used for imaging areas larger than 50 × 50 μm, and the piezo positioning system was used otherwise. A manual switch was connected between the leads of the potentiostat and the substrate electrode to avoid any electrical spike that can arise on switching that could damage the TiO_2 passivation layer.

Spectroelectrochemical Measurements. A fresh sol-ution of 0.5 mM CTC in 0.1 M phosphate buffer pH 7 was prepared before each experiment. Experiments were performed on an inverted microscope (Olympus IX-71) with an Olympus 100× oil-immersion objective with variable N.A. (0.6−1.3). A homemade spectroelectrochemical cell with a No.1 thickness microscope coverslip (Fisher) as the bottom was used due to the short working distance of the objective. The working electrode (Pt UME), counter electrode (Pt wire), and reference electrode (Ag/AgCl KCl 1M) were positioned in the cell with a custom holder and manual micropositioning system that allowed for the working electrode to be consistently positioned between 150 and 200 μm from the spectroelectrochemical cell surface. A CHI650E potentiostat from CH Instruments (Austin, TX) was used to carry out the electrochemistry. After CTC reduction, the electrode was illuminated with circularly polarized 532 nm laser excitation (Spectra-Physics, 532−50-CDRH) in an epi-illumination configuration with an intensity of approximately 0.1 kW/cm^2. Fluorescence emission was filtered through a dichroic/long-pass/notch filter combi-nation with a cutoff near 540 nm (Semrock) before being directed onto an electron-multiplied CCD detector (ProEM, Princeton Instruments). All movies were collected with an integration time of 100 ms over the entire CCD chip.

Electro-Active Defect Counting. Estimating the number of electro-active defects on the electrode was performed by an in-house written MATLAB code based on local maxima. Prior to calculating the local maxima, the first 20 frames of the recorded fluorescence from electro-active defects were summed to increase the signal-to-noise ratio and smooth the spot profile. A threshold was then set at background intensity plus three times the background standard deviation. Pixels with intensity above the threshold were then compared with their 48 nearest neighbors. If the pixel intensity was higher than 47 of the 48 nearest pixels, it was considered a local maximum. Local maxima that were within five pixels of each other (based upon the fwhm of spatially resolved electro-active defects) were counted as a single electro-active defect. Each camera pixel represents 59 nm. Electro-active defect quantities determined by the algorithm described above were comparable to manual counting of suspected defects.

Electrode Passivation. The electrodeposition of amor-phous TiO_2 was performed as described in the literature.[8] $TiCl_3$ solution for the electrodeposition of TiO_2 was prepared by diluting 12% $TiCl_3$ solution in HCl 1:20 in deionized water, followed by pH neutralization to 2.45 ± 0.03 by addition of 0.5 M $NaHCO_3$ solution. The solution color turned from pink to deep purple upon pH neutralization. The final solution Ti concentration was ca. 15 mM. The electrodeposition process was performed by application of 0.02 V vs SCE. For a typical

deposition cycle, 40 s potential application time was chosen. The deposited TiO_2 film was dried thoroughly under a microscope lamp for 10 min after each deposition cycle. Deposition progress was monitored by taking a cyclic voltammogram of the electrode in a 1 mM ferrocenemethanol solution (see Figure S1 in Supporting Information). Multiple deposition cycles were carried out to ensure sufficient level of surface passivation. Deposition solutions were freshly made prior to an experiment, and no solution older than 1 h was used.

■ RESULTS AND DISCUSSION

Observation of Electro-Active Surfaces by Fluorescence Microscopy and SECM. Figure 1 shows the
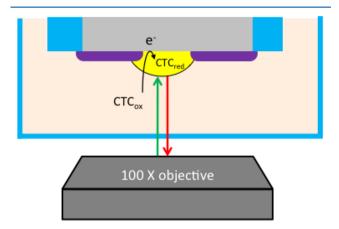

Figure 1. Schematic of the spectroelectrochemical setup. The blue, light orange, and gray colors correspond to glass (electrochemical cell and UME sheath), the CTC_{ox} solution, and the Pt electrode, respectively. The violet and yellow colors represent an insulating thin layer and a deposit of solid CTC_{red} at a defect site, respectively. A 532 nm laser (green arrow) in epi-illumination excites fluorescence through the objective, while emission of the CTC_{red} (red arrow) is collected by the same objective and sent to the detector.

spectroelectrochemical setup used to observe electro-active surfaces by fluorescence microscopy. The UME is positioned above a high numerical aperture microscope objective in a home-built spectroelectrochemical cell made with a microscope coverslip as the bottom window so that an image of the surface of interest in the UME can be collected. The cell contains 0.5 mM of oxidized CTC (CTC_{ox}), a redox-active species that is nonfluorescent in its oxidized form. Upon production of the reduced form (CTC_{red}) the species becomes strongly fluorescent in the visible (λ_{em} = 665 nm). The chemical structures of CTC_{ox} and CTC_{red} are provided in Figure 2 and the fluorescence spectra of CTC_{ox} and CTC_{red} are provided in Figure S2 in Supporting Information. A change in the redox state of the CTC can thus easily be tracked by fluorescence microscopy. This property has been exploited in the field of biochemistry to track reducing species generated inside living cells.[29] Another important characteristic of CTC is a change of solubility upon reduction. While CTC_{ox} is positively charged and soluble in water, CTC_{red} is a neutral species insoluble in water. The fluorescent CTC_{red} is therefore expected to deposit on the electro-active surface at the site where it has been reduced, as depicted in Figure 1 (yellow color). We checked this behavior by reducing CTC on an unpassivated electrode and recording a movie (see Movie S1 in Supporting
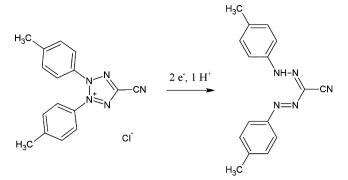

Figure 2. Chemical structure of CTC_{ox} being irreversibly reduced to CTC_{red}.

Information) of the fluorescence at the surface of the electrode. The Movie S1 shows that CTC_{red} is effectively electrodeposited at the surface of electrode and does not diffuse away or get ejected from the electrode due to electric potential changes. This is an important point with respect to lateral resolution. Zhang and co-workers showed by using a soluble fluorescent dye, resazurin, that the fluorescence signal recorded at an electrode surface broadens with time due to diffusion.[30] The use of a water insoluble fluorescent dye like CTC allows for the spatial resolution to be independent of diffusion. It also offers the possibility to independently carry out the electrodeposition of the dye before performing the fluorescence measurement.

To test if our spectroelectrochemical technique is effectively able to image the electro-activity of a surface, we used the well-defined electro-active surface of 25 μm diameter Pt UMEs as a standard. The Pt surface was polished with diamond paper (0.1 μm grit) and dipped in a piranha solution to obtain reproducible and clean surfaces. Figure 3a shows a cyclic voltammogram corresponding to the oxidation of 5 mM 1,1′-ferrocenedimethanol (FcDM) on a bare Pt UME. The steady
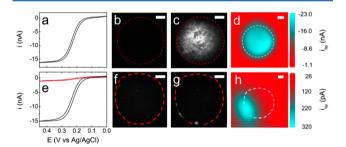

Figure 3. Data shown in the top and bottom rows are obtained with a bare 25 μm diameter Pt UME and a θ = 94.8% passivated 25 μm diameter Pt UME, respectively. (a, e) Cyclic voltammograms measured at 20 mV/s in a solution of 5 mM FcDM with 0.1 KNO_3. The black line represents the CV of the FcDM from a bare electrode, while the red curve (e only) shows the CV from the same electrode after passivation with TiO_2. (b, f) Fluorescence micrographs measured at 0.2 V, before reduction of CTC. (c, g) Fluorescence micrographs measured at 0.2 V, after application of −0.6 V for 5 s (c) and 15 s (g) to deposit CTC on the electrode. (d, h) SECM images of the Pt UMEs. The SECM image in (d) was recorded in feedback mode with E_{tip} = 0.4 V, E_{sub} = 0.0 V, a tip−substrate distance of 1.8 μm, and a scanning rate of 2.5 μm/s. The SECM image in (h) was recorded in generation-collection mode with E_{tip} = 0 V, E_{sub} = 0.4 V, a tip−substrate distance of 3.7 μm and a scanning rate of 2.5 μm/s. Scale bars = 5 μm. [FcDM] = 4.7 mM; the dashed lines indicate the position of the Pt electrode.

state current, i_{ss}, is related to the radius of the electrode, r_{elec}, by the relation:[23]

$$i_{ss} = 4nFDC \times r_{elec} \qquad (1)$$

where n is the number of electrons exchanged, F is Faraday's constant, D is the diffusion coefficient, and C^* is the bulk concentration. The value of D for FcDM is taken as 6.7×10^{-6} cm^2/s.[31] Eq 1 provides a way to monitor electrochemically the apparent size of the electro-active surface. For the electrode shown in Figure 3a, the value of r_{elec} is 26 ± 1 μm, in agreement with the value measured optically (26 ± 1 μm). A fluorescence micrograph of the electrode before reduction of CTC is shown in Figure 3b. No fluorescence signal is observed, indicating that there is no reduced CTC at the surface of the UME (glass and Pt). The electrode is then biased at -0.6 V for 5 s in a 0.5 mM CTC$_{ox}$ solution. At this potential the CTC is irreversibly reduced on Pt (see Figure S3). The chronoamperogram corresponding to the reduction of CTC on the UME is provided in Figure S4 in Supporting Information. Immediately after the reduction/deposition of CTC, a fluorescence micrograph of the electrode (Figure 3c) is recorded. A large number of individual fluorescent spots are observed at the Pt surface. However, no fluorescence is observed on the insulating glass sheath. The size of the fluorescent spots (in Figure 3C), defined as the fwhm of a Gaussian function adjusted on the intensity profile of a spot, is about 550 ± 70 nm, which corresponds to the optical resolution of our setup. We observe that the longer the electrodeposition time, the broader the spots appear (Movie S1, Supporting Information), indicating a continuous deposition of the CTC$_{red}$ on the electrode. The electrodeposition time (2−15 s) was thus optimized to maximize the intensity of fluorescence and the spatial resolution. The brighter intensity at the center of the electrode observed in Figure 3c is caused by the intensity profile of the excitation laser spot which is more intense at the center of the beam than the edges and, therefore, results in brighter emission observed at the electrode center.

The reactivity of the UME was also imaged by a scanning probe technique, SECM. The SECM experiment was carried out before the CTC reduction to start with a clean bare Pt surface. The SECM image shown in Figure 3d was recorded at 1.8 μm from the electrode surface with a 10 μm gold UME (RG = 2−3). The approach curve is shown in Figure S5 in Supporting Information. The redox probe, FcDM (4.7 mM in 0.1 M KNO$_3$), was oxidized to FcDM$^+$ at the Au tip and reduced back to FcDM at the Pt substrate. When the Au tip is scanned over an insulating material (e.g., glass sheath) the diffusion of FcDM at the tip is hindered and a decrease in current is expected (negative feedback). On the other hand a conducting substrate will regenerate FcDM$^+$ to FcDM and thus increase the current (positive feedback). As expected, a large positive feedback (blue color in Figure 3d) is observed when the tip is scanned above the Pt electrode while negative feedback (red color in Figure 3d) is observed above the insulating glass sheath. The comparison of the SECM and fluorescence pictures shown in Figure 3c and d, respectively, clearly indicates that the fluorescence spots are only observed on the electro-active Pt surface. This result demonstrates that a conducting area of several hundreds of μm^2 can be readily imaged using CTC and fluorescence microscopy.

Electro-active surfaces smaller than 25 μm diameter were also studied using the following strategy. A bare 25 μm diameter Pt UME was partially passivated by electrodeposition of an insulating layer of TiO$_2$. Details on the electrodeposition of TiO$_2$ are provided in the Experimental Section and in Supporting Information. By controlling carefully the time of electrodeposition, a few defects can be left in the insulating layer. Figure 3e shows the cyclic voltammograms corresponding to the oxidation of 5 mM FcDM at a Pt UME before (black trace) and after (red trace) passivation with TiO$_2$. After passivation, the steady state current is considerably lower indicating that a significant portion of the surface of the electrode is blocked. The remaining faradaic current is due to electro-active defects left in the TiO$_2$ layer. The degree of blocking of the current, θ, was quantified using the following relation:

$$\theta = 100 \times \left(1 - \frac{i_{ss}^{TiO_2}}{i_{ss}}\right) \qquad (2)$$

where $i_{ss}^{TiO_2}$ is the steady state current of the electrode after passivation. A value of $\theta = 0\%$ corresponds to a bare Pt UME and a value of $\theta = 100\%$ corresponds to a fully passivated electrode with no electro-active defects. The voltammogram in Figure 3e corresponds to an electrode with θ equal to 94.8%. The passivated electrode was studied following the same protocol that was used for the bare UME. Fluorescence micrographs were recorded before (Figure 3f) and after (Figure 3g) the CTC reduction. A couple of dim spots can be observed in Figure 3f before CTC reduction. In contrast to the fluorescence spots associated with CTC deposition that can be photobleached by the laser, these dim spots do not fade upon illumination (see Figure S6), nor do they have the CTC emission profile (Figure S2). The dim spots are thus not attributed to fluorescence and can be easily removed from the analysis by subtracting the "before" image (Figure 3f) from the "after" image (Figure 3g). We suspect they come from light scattered by topographic defects, which are not electro-active based on lack of evidence of CTC deposition at these sites. After the reduction of CTC, a few individual fluorescent spots can be seen on the bottom left perimeter of the UME (indicated with the dashed lines in Figure 3g). We confirmed that the signal coming from these spots is CTC fluorescence due to the expected photobleaching (see Figure S6). These spots spread over an about 20 μm line at the junction between the glass and the Pt and their fwhm is about 800 nm, slightly larger than the imaging resolution of the microscope.

The electro-activity of the electrode was also imaged by SECM. The SECM image of the electrode surface is shown in Figure 3h. The image was recorded using a 10 μm diameter Au tip (RG = 2−3) and 4.7 mM FcDM in 0.1 M KNO$_3$. Imaging was carried out at a distance of 3.7 μm from the surface (see approach curve Figure S7 in Supporting Information) in generation-collection mode. The Pt substrate is biased at 0.4 V to generate FcDM$^+$ and the Au tip is biased at 0 V to collect the FcDM$^+$. In this particular imaging mode, an insulating substrate will give no current, and a conducting surface will induce a cathodic current at the tip. The SECM image Figure 3h evidence FcDM$^+$ coming from the same location where fluorescence is observed in Figure 3g. Because a 10 μm Au tip was used to image the surface of the electrode, the resolution of the SECM image is not high enough to finely compare the location of the electro-active spots. Multiple attempts to image the Pt UME with a 1 μm diameter tip were made but topographic defects on the UME surface repeatedly damaged the tip during the imaging. Altogether, these results

prove that electro-active surfaces can be imaged by fluorescence via CTC reduction, even for submicron electro-active defects.

As mentioned above, the CTC_{red} is insoluble in aqueous solutions, but soluble in organic solutions. In an attempt to remove the CTC_{red} from the electrode surface, we submerged the electrode into DMSO at 25 °C and gently stirred the solution for 45 min. An electrode with CTC_{red} on the surface shows an increased capacitance and current response when cycling in FeMeOH. After cleaning with DMSO, we would observe the electro-response of the electrode return to that of before the reduction of CTC. Unfortunately, reducing CTC on the cleaned electrode did not reproduce the original fluorescent signal. The difficulty for completely removing the CTC_{red} from the surface might be due to the reduction of the molecule by electrochemical methods. Previous electrochemical studies of CTC analogues evidenced the formation of radicals.[32,33] These radicals might react together or with the electrode to form a robust fluorescent CTC_{red} layer. Nevertheless the fluorescence signal of this CTC_{red} layer decreases upon exposure to the laser beam. By using photobleaching the fluorescent signal can be completely muted if necessary. Methods to remove the CTC_{red} and make our proposed method completely nondestructive are currently under investigation.

Localization and Sizing of Electro-Active Defects. Figure 4a shows a fluorescence micrograph of a passivated UME with $\theta = 91.4\%$ after electrodeposition of CTC. In order to analyze this kind of fluorescence image, some assumptions need to be made. First, each fluorescent spot can correspond either to multiple small electro-active defects closer than ~550 nm (fwhm of a spot) or one single large electro-active defect. For the sake of simplicity, we will assume that each spot corresponds to one electro-active defect that is circular in shape. Based on this assumption the micrograph shown in Figure 4a was analyzed with a home-written MATLAB program to locate and count local intensity maxima. Details about the MATLAB code are provided in the Experimental Section. The position of each fluorescence spot detected by the program is indicated in Figure 4b by the red circles. The number of fluorescent spots, which is assumed to reflect the number of electro-active defects, N_{def}, is 64 in this case. The center of the fluorescent spots can be measured with a precision of about 59 nm (the size of a pixel on the CCD chip). Note that because of the assumption made previously, N_{def} is a lower bound of the actual number of defects. The advantage of measuring the entire surface of the sample is the possibility to reliably estimate the distribution of electro-active defects. In the case shown in Figure 4a, the electro-active defects are obviously not distributed homogeneously over the surface of the electrode (indicated by the red dotted line in Figure 4a,b). The fluorescence micrograph shown in Figure 3g displays an even more inhomogeneous distribution of defects with, in that particular case, defects located only at the junction between the Pt and the glass. With such an inhomogeneous distribution, the density of defects calculated by simply dividing N_{def} by the electrode surface does not accurately reflect the sample properties. Only the analysis of the full sample will provide an accurate description of the electro-active defects distribution. Note that scanning probe techniques are typically measuring small areas taken randomly over the sample surface, which could lead to large errors in the density and distribution of defects.

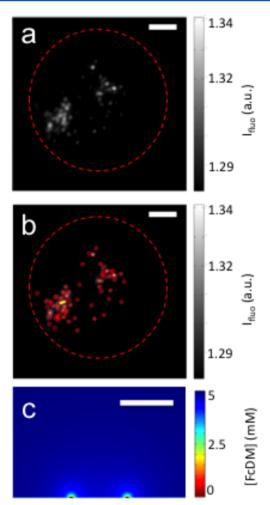Another important characteristic of the electro-active defect is their size. The size of the fluorescent spots in our

Figure 4. (a) Fluorescence micrograph of a passivated UME with $\theta = 91.4\%$ after deposition of CTC. (b) Same fluorescence micrograph from (a) with the position of all the fluorescence local maximum (red circles) detected by the Matlab program. The yellow line indicates the position of the two electro-active defects used to define the geometry of the simulation shown in (c). The red dashed lines indicate the position of the Pt electrode and the scale bars correspond to 5 μm. (c) Side view of the concentration profile of FcDM at two 33 nm radius electro-active defects (located at the origin of the color gradient, on the bottom of the figure) spaced by 1 μm (center to center) assuming mass transfer limited conditions and a 1 s long experiment. Details about the simulation are provided in Supporting Information. The scale bar corresponds to 1 μm.

fluorescence micrographs is close to the optical diffraction limit and thus electrochemistry, in combination with the fluorescence imaging, was used to determine the size of electro-active spots. The value of i_{ss} measured with the passivated electrode depends on the radius, r_{def}, of all the defects present in the passivation layer and the distance, d_{def}, between adjacent defects. If the defects are far enough from each other compared to their radius ($d_{def} \gg r_{def}$), then the diffusion layers of individual defects do not overlap significantly. In that case, the current from each defect is simply given by eq 1. However, if the two electro-active defects are close enough to each other to have a significant overlap of their diffusion layer, then the apparent radius of the electro-active defects is different from their real radius.[34] Another factor that can affect the current is the thickness of the insulating film. If the film is thick relative to the size of the electro-active defects then the electro-active

defects will behave like a recessed electrode and the current will be lower than expected for an electrode perfectly inlaid with the insulating surrounding.[35] For a quantitative analysis the thickness of the insulating layer should be determined independently. In our particular case we only aim at a semiquantitative analysis and thus we assume an extremely thin TiO_2 insulating layer.

To determine the size of the electro-active defects we first assume independent defects. The total current is then the sum of the current coming from each individual defect. Since the electrochemical measurement simultaneously probes all defects, an average value of the radius of electro-active defects, r_{ave}, is obtained using the following equation:

$$i_{ss} = 4nFDC \times \sum_{j=0}^{N_{def}} r_{def,j} = 4nFDC \times N_{def} r_{ave}$$

(3)

Note that N_{def} is a minimum estimate and thus the value of r_{ave} represents an upper estimate of the average defect radius. In the case shown in Figure 4a, i_{ss} = 2.8 nA, C^* = 5.1 mM, and N_{def} = 64. Using these parameters and eq 3, we calculated r_{ave} = 33 nm. To verify if the assumption of noninteracting electrodes is reasonable, we carried out a numerical simulation of two 33 nm radius electrodes spaced (from center to center) by 1 μm. This distance corresponds to the distance between the two electro-active defects along the yellow line drawn in Figure 4b and represents a conservative estimate of d_{def}. A concentration profile of FcDM along the yellow line after 1 s of mass transfer limited oxidation is shown in Figure 4c. Details about the simulation are provided in Supporting Information. Figure 4c shows a low overlap between the diffusion layers of the two electro-active defects. This overlap leads to only a 2% difference in the current obtained for two completely independent 33 nm radius electrodes. The assumption of noninteracting electrode is thus reasonable for the case shown in Figure 4. An additional numerical simulation of two defects spaced by 300 nm predicts a crosstalk of only 6% between the defects. With a value of r_{ave} of 33 nm and an experimental minimum distance between defects of 300 nm (the optical resolution of our system) the effect of the crosstalk on r_{ave} is thus negligible. Note that for larger defects that are separated by less than a micron, numerical simulations could be used to estimate the value of r_{ave} in the case of interacting electrodes.

The interesting result is that the value of r_{ave} obtained by combining electrochemistry and fluorescence microscopy is well below the optical diffraction limit. The smallest average defect radius observed with the proposed spectroelectrochemical technique is 9 nm (the corresponding fluorescence micrograph is shown in Figure 4b). Here, the high sensitivity and spatial resolution of fluorescence microscopy combined with the quantitative capability of electrochemistry enables us to localize and size a 9 nm average radius electro-active defect in less than 15 min over a 490 μm^2 sample.

Analysis of Electro-Active Defects in Electrodeposited Insulating TiO_2 Layer. Here, we use the previously described spectroelectrochemical technique to study electro-active defects in electrodeposited TiO_2 layers. Figure 5 shows fluorescence micrographs of passivated 25 μm diameter Pt electrodes with θ = 99.8, 91.4, and 0% (from top to bottom row) before (left column) and after (middle column) CTC reduction. The right column images are all on the same intensity scale as Figure 5a to better demonstrate the increasing fluorescence signal with decreasing TiO_2 surface coverage. No fluorescence signal is
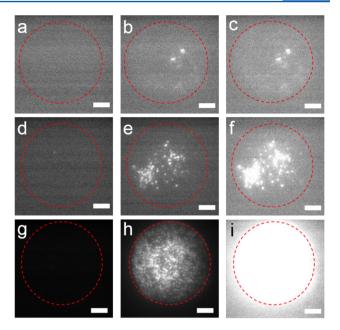

Figure 5. Fluorescence micrographs of TiO_2 passivated UMEs with θ values of 99.8% (a–c), 91.4% (d–f), and 0% (g–i). The micrographs in the left and center columns were taken before and after reduction of CTC, respectively. The right column images are all put onto the same intensity scale as (a). All scale bars represent 5 μm.

detected on the surface of the electrodes before CTC reduction (the electrode position is indicated by the red line). However, after CTC reduction multiple fluorescent spots are clearly observed. The spectroelectrochemical data corresponding to the electrodes shown in Figures 4 and 5 and other electrodes (see Figure S8 in Supporting Information) was quantitatively analyzed using the procedure described in the previous section. The parameters θ, N_{def}, d_{def}, i_{ss}, and r_{ave}, are gathered in Table 1.

Table 1. Spectroelectrochemical Analysis of TiO_2 Passivated Electrodes

θ (%)	N_{def}	d_{def} (μm)	i_{ss} (nA)	r_{ave} (nm)
		25 μm Diameter Pt UME		
99.8	4	3	0.05	9
99.6	1		0.07	90
92.4	45	1	1.30	40
91.4	64	1	2.79	33
		1.3 μm Diameter Pt UME[a]		
99.9			0.002	1
99.8			0.004	2
99.7			0.006	3

[a]The value of i_{ss} was measured using a 10 mM FcDM solution.

General trends are observed; there is an inverse relationship between θ and the number of fluorescent spots observed, in agreement with a larger amount of electro-active defects expected for lower passivation. For the range of θ values examined (99.8–91.4%), r_{ave} has a median value of 40 nm and no trend is observed. For high coverage (large value of θ) the average size of the defects bears more uncertainty. This is due to the low number of defects that makes statistical analysis less reliable. Note also that higher coverage means longer electrodeposition time and thus thicker films. As mentioned previously a variation of the thickness can affect the value of r_{ave}. The absence of a significant trend in average defect size

might be an indication that the electro-active defects in the TiO_2 film are caused by surface defects on the original Pt electrode, with the size of these surface defects being relatively constant between electrodes and polishing. The surface of the TiO_2 passivated electrodes was imaged by scanning electron microscopy (SEM) to evidence topographic/insulating defects. When the surface of the electrode presents large topographic defects (>μm) we observed a correlation between the location of the electro-active defects observed in the fluorescence images and the topographic defects observed by SEM (see Figure S9). However, for electrodes with apparently smooth surfaces based on the SEM images, no correlation between reactivity and topography could be established.

To test the limit of our spectroelectrochemical method we also used laser pulled Pt UMEs with 1.3 μm diameters as substrates, which were milled by focused ion beam. The small and smooth surface of these UMEs reduces the probability of having defects and nearly complete passivation with ~1 nm thickness of TiO_2 can be obtained after its electrodeposition.[36] Figure 6 shows fluorescence micrographs of a bare ($\theta = 0\%$)
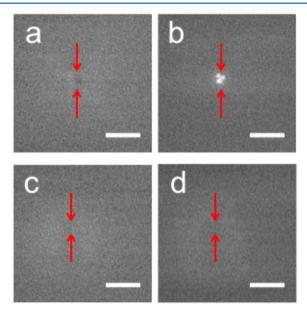

Figure 6. Fluorescence micrographs of (a, b) a bare 1.3 μm diameter Pt UMEs ($\theta = 0\%$) and (c, d) a 1.3 μm diameter Pt UME passivated with a thin layer of TiO_2 ($\theta = 99.7\%$). The micrographs in the left and right columns were taken before and after reduction of CTC, respectively. All scale bars represent 5 μm. The red arrows indicate the position of the UME.

(top row) and a $\theta = 99.9\%$ passivated UME (bottom row). The position of the electrode is indicated with the red arrows. The left and right column show fluorescence micrographs recorded before and after electrodeposition of CTC, respectively. Before CTC reduction no fluorescence is detected (see Figure 6a,c). After reduction of CTC the bare Pt UME exhibits strong fluorescence (see Figure 6b). As already observed with 25 μm Pt UME, the CTC is reduced on distinct seeding sites of the UME. The passivated UME with $\theta = 99.9\%$ does not produce any detectable fluorescence signal (see Figure 6d). Similar experiments carried out with two other UMEs ($\theta = 99.8$ and 99.7%, Figure S8b,c) also did not show fluorescence. Assuming a single electro-active defect in the TiO_2 layer we used the steady state current of a 10 mM FcDM solution to estimate the

size of a potential defect. As shown in Table 1 for each electrode, the defect would be smaller than ~6 nm in diameter. This very conservative calculation tends to indicate that electro-active defects smaller than about 6 nm in diameter do not produce a detectable fluorescence signal under our experimental conditions, although they can be estimated by voltammetry at high current sensitivities.

■ CONCLUSION

In summary, we have developed a far-field optical technique, based upon combining fluorescence microscopy and electrochemistry, capable of imaging electro-active defects in insulating layers. This technique was compared and validated with a scanning probe technique, SECM. Hence, we demonstrate that CTC is a suitable fluorescent redox dye for probing the reactivity of surfaces via fluorescence. Semiquantitative analysis of the substrate can be readily achieved, and important parameters such as the minimum number and the location of the defects can be extracted from the fluorescence data. An average size of the defects can also be estimated from the combination of the fluorescence and electrochemical data. This far field technique allows imaging large areas (hundreds of μm^2) quickly (less than 15 min) without sacrificing spatial resolution. The study of electrodeposited TiO_2 passivating layers revealed the presence of electro-active defects with an average size of only few tens of nanometer scattered over a sample of 490 μm^2. Interestingly we found that the electro-active defects are not homogeneously distributed over the Pt surface, and only the analysis of the entire sample can provide an accurate description of the electro-active defect distribution. Another interesting aspect of this technique is the versatility of the substrate that can be imaged. Since there is no scanning probe involved (as with c-AFM or SECM), samples with high roughness can be imaged without risk of collision that could damage both the probe and the sample. Note also that depending on the size of the electro-active defects, the scale of the analysis can be adjusted by changing the objective of the microscope. This technique represents a simple semiquantitative alternative to other time intensive techniques like c-AFM and SECM, and we believe that it can be applied for a large variety of substrates and insulating layers. However, defects smaller than about 6 nm are not imaged. Their presence can be detected electrochemically, so the combined methods produce complementary information about defects in blocking films.

■ ASSOCIATED CONTENT

ⓢ Supporting Information

Blocking of the UME with TiO_2, absorption and emission spectra of CTC_{ox} and CTC_{red}, voltammogram of CTC at a Pt electrode, chronoamperogram for the electrodeposition of CTC on a Pt UME, approach curves for the SECM pictures, photobleaching measurements, fluorescence micrographs of Pt UMEs after CTC deposition, comparison of SEM and fluorescence pictures and details for the numerical simulation. The Supporting Information is available free of charge on the ACS Publications website at DOI: 10.1021/acs.analchem.5b00898.

■ AUTHOR INFORMATION

Corresponding Authors
*E-mail: ajbard@cm.utexas.edu.
*E-mail: kwillets@temple.edu.

Present Address

§Department of Chemistry, Temple University, 1901 N. 13th. St., Philadelphia, Pennsylvania 19122, United States (K.A.W.).

Author Contributions

†These authors contributed equally to the work (C.R. and K.M.).

Notes

The authors declare no competing financial interest.

■ REFERENCES

(1) Zhou, L.; Zhuang, J. Y.; Tongay, S.; Su, W. M.; Cui, Z. *J. Appl. Phys.* **2013**, *114*, 074506.

(2) Kim, H.; Lee, H.-B.-R.; Maeng, W.-J. *Thin Solid Films* **2009**, *517*, 2563−2580.

(3) Meena, J. S.; Chu, M.-C.; Singh, R.; Shieh, H.-P. D.; Liu, P.-T.; Ko, F.-H. *J. Mater. Sci: Mater. Electron.* **2013**, *24*, 1807−1812.

(4) Suemori, K.; Uemura, S.; Yoshida, M.; Hoshino, S.; Kodzasa, T.; Kamata, T. *Thin Solid Films* **2008**, *516*, 2739−2742.

(5) Roy, T.; Tosun, M.; Kang, J. S.; Sachid, A. B.; Desai, S. B.; Hettick, M.; Hu, C. C.; Javey, A. *ACS Nano* **2014**, *8*, 6259−6264.

(6) Chen, Y. W.; Prange, J. D.; Dühnen, S.; Park, Y.; Gunji, M.; Chidsey, C. E. D.; McIntyre, P. C. *Nat. Mater.* **2011**, *10*, 539−544.

(7) Liu, R.; Zheng, Z.; Spurgeon, J.; Yang, X. *Energy Environ. Sci.* **2014**, *7*, 2504−2517.

(8) Eisenberg, D.; Ahn, H. S.; Bard, A. J. *J. Am. Chem. Soc.* **2014**, *136*, 14011−14014.

(9) Seger, B.; Pedersen, T.; Laursen, A. B.; Vesborg, P. C. K.; Hansen, O.; Chorkendorff, I. *J. Am. Chem. Soc.* **2013**, *135*, 1057−1064.

(10) Seger, B.; Tilley, D. S.; Pedersen, T.; Vesborg, P. C. K.; Hansen, O.; Grätzel, M.; Chorkendorff, I. *RSC Adv.* **2013**, *3*, 25902−25907.

(11) Wink, T.; van Zuilen, S. J.; Bult, A.; van Bennekom, W. P. *Analyst* **1997**, *122*, 43R−50R.

(12) Xiao, Y.; Lai, R. Y.; Plaxco, K. W. *Nat. Protocols* **2007**, *2*, 2875−2880.

(13) Shchukin, D. G.; Zheludkevich, M.; Yasakau, K.; Lamaka, S.; Ferreira, M. G. S.; Möhwald, H. *Adv. Mater.* **2006**, *18*, 1672−1678.

(14) Chai, Z.; Liu, Y.; Li, J.; Lu, X.; He, D. *RSC Adv.* **2014**, *4*, 50503−50509.

(15) Satpati, A. K.; Arroyo-Currás, N.; Ji, L.; Yu, E. T.; Bard, A. J. *Chem. Mater.* **2013**, *25*, 4165−4172.

(16) Isaacs, H. S.; Davenport, A. J.; Shipley, A. *J. Electrochem. Soc.* **1991**, *138*, 390−393.

(17) Schmutz, P.; Frankel, G. S. *J. Electrochem. Soc.* **1998**, *145*, 2285−2295.

(18) Wittmann, M. W.; Leggat, R. B.; Taylor, S. R. *J. Electrochem. Soc.* **1999**, *146*, 4071−4075.

(19) Lang, K. M.; Hite, D. A.; Simmonds, R. W.; McDermott, R.; Pappas, D. P.; Martinis, J. M. *Rev. Sci. Instrum.* **2004**, *75*, 2726−2731.

(20) Dobson, P. S.; Weaver, J. M. R.; Holder, M. N.; Unwin, P. R.; Macpherson, J. V. *Anal. Chem.* **2004**, *77*, 424−434.

(21) Sun, L.; Crooks, R. M. *J. Electrochem. Soc.* **1991**, *138*, L23−L25.

(22) Bard, A. J.; Fan, F.-R. F.; Pierce, D. T.; Unwin, P. R.; Wipf, D. O.; Zhou, F. *Science* **1991**, *254*, 68−74.

(23) Bard, A. J.; Mirkin, M. V. Scanning Electrochemical Microscopy, 2nd ed.; CRC Press: New York, 2012.

(24) Patten, H. V.; Meadows, K. E.; Hutton, L. A.; Iacobini, J. G.; Battistel, D.; McKelvey, K.; Colburn, A. W.; Newton, M. E.; Macpherson, J. V.; Unwin, P. R. *Angew. Chem., Int. Ed.* **2012**, *51*, 7002−7006.

(25) Basame, S. B.; White, H. S. *J. Phys. Chem. B* **1998**, *102*, 9812−9819.

(26) Basame, S. B.; White, H. S. *Anal. Chem.* **1999**, *71*, 3166−3170.

(27) Serebrennikova, I.; White, H. S. *Electrochem. Solid-State Lett.* **2001**, *4*, B4−B6.

(28) Serebrennikova, I.; Lee, S.; White, H. S. *Faraday Discuss.* **2002**, *121*, 199−210.

(29) Bhupathiraju, V. K.; Hernandez, M.; Landfear, D.; Alvarez-Cohen, L. *J. Microbiol. Methods* **1999**, *37*, 231−243.

(30) Oja, S. M.; Guerrette, J. P.; David, M. R.; Zhang, B. *Anal. Chem.* **2014**, *86*, 6040−6048.

(31) Zevenbergen, M. A. G.; Singh, P. S.; Goluch, E. D.; Wolfrum, B. L.; Lemay, S. G. *Anal. Chem.* **2009**, *81*, 8203−8212.

(32) Umemoto, K. *Bull. Chem. Soc. Jpn.* **1989**, *62*, 3783−3789.

(33) Oritani, T.; Fukuhara, N.; Okajima, T.; Kitamura, F.; Ohsaka, T. *Inorg. Chim. Acta* **2004**, *357*, 436−442.

(34) Gueshi, T.; Tokuda, K.; Matsuda, H. *J. Electroanal. Chem. Interfacial Electrochem.* **1978**, *89*, 247−260.

(35) Bartlett, P. N.; Taylor, S. L. *J. Electroanal. Chem.* **1998**, *453*, 49−60.

(36) Kim, J.; Kim, B.-K.; Cho, S. K.; Bard, A. J. *J. Am. Chem. Soc.* **2014**, *136*, 8173−8176.